Composites Science and Technology 230 (2022) 109729

Contents lists available at ScienceDirect

Composites Science and Technology

journal homepage: www.elsevier.com/locate/compscitech

An efficient stiffness degradation model for layered composites with arbitrarily oriented tunneling and delamination cracks

Leon Herrmann [a,*], Lars P. Mikkelsen [b,*], Brian N. Legarth [c], Fabian Duddeck [d], Christian F. Niordson [c]

[a] Chair of Computational Modeling and Simulation, Technical University of Munich, D-80333 Munich, Germany
[b] Department of Wind and Energy Systems, Technical University of Denmark, DK-4000 Roskilde, Denmark
[c] Department of Civil and Mechanical Engineering, Solid Mechanics, Technical University of Denmark, DK-2800 Kgs. Lyngby, Denmark
[d] Chair of Computational Mechanics, Technical University of Munich, D-80333 Munich, Germany

ARTICLE INFO

Keywords:
Stiffness estimation
Finite element method
Ply discount estimate
Composite laminates
Homogenization
Nondestructive damage identification

ABSTRACT

A periodic 2D finite element model is proposed to identify the axial and transverse stiffness degradation for arbitrarily oriented parallel tunneling cracks. This is achieved with a recently developed off-axis framework taking the 3D deformation into account via a special kinematic formulation. The proposed model is successfully validated against a variety of cases from the literature. Not only is the model capable of accurately predicting what previously was only possible with expensive 3D models or complex analytical methods, but at the same time, it is achieved with remarkably small finite element models which only take seconds for each simulation. A parametric study, shows that by including frictionless contact between the crack surfaces, a significant effect on the stiffness degradation is present for carbon fiber composite materials for off-axis orientations below 40°. An effect not seen for the analyzed glass fiber composites. In addition, based on the axial and transverse stiffness degradation, a method is proposed from which the amount of simultaneous tunnel cracking and delamination can be predicted. A Fortran-based user subroutine and supplementary Python scripts for the commercial finite element code Abaqus are made available as a co-published data-repository reference.

1. Introduction

Fiber-reinforced composites have become highly desirable materials in a variety of industries, due to their high strength and stiffness to weight ratios. During their lifetime, they experience several damage mechanisms. To ensure safety and reliability in their usage, it is essential, that these mechanisms are understood. They can be described in three stages [1–3], which are illustrated in Fig. 1 for a [0/90] layup. In the first stage, Fig. 1(a), tunneling cracks (marked in red), initiate in the off-axis layers, i.e. in this case the 90°-layer, and tunnel along the fiber direction. This occurs in a sequential manner leading to a distribution of tunneling cracks. The cracks lead to stress concentrations at the interface to the neighboring plies, which then leads to decohesion of the layers (marked in blue). In Fig. 1(b), this second stage is referred to as delamination. Finally, as shown in Fig. 1(c), the damage in the off-axis layers weakens the entire laminate sufficiently, that fiber breakage in the load-carrying layers occur in the third stage. The fiber breakage leads to fiber-pullout and full separation of the laminate, i.e. the ultimate collapse of the laminate.

Important for the deployment of fiber-reinforced composites is not only the prediction of their lifetime but also of their performance. In particular, the stiffness degradation caused by the damage mechanisms is of interest, as the stiffness itself is very often important to the structural safety of a component. Furthermore, the stiffness degradation may be used to monitor the amount of internal damage, thus contributing to accurate lifetime predictions. For this purpose measurements of the degradation of multiple stiffness components can be used in combination with computationally cheap stiffness prediction methods. This enables a unique identification of the progression of the different damage stages. It is in this work illustrated by considering the combined impact from tunneling and delamination cracks on the stiffness degradation. The presented damage identification approach can however also be used to include the stiffness degradation effect from fiber-breakage.

A variety of tools [4–7] exists to determine the stiffness degradation due to both tunneling, and delamination cracks. A good overview is provided in [8], where analytical, semi-analytical, numerical, and

* Corresponding authors.
E-mail addresses: leon.herrmann@tum.de (L. Herrmann), lapm@dtu.dk (L.P. Mikkelsen).

https://doi.org/10.1016/j.compscitech.2022.109729
Received 15 January 2022; Received in revised form 13 July 2022; Accepted 5 September 2022
Available online 21 September 2022

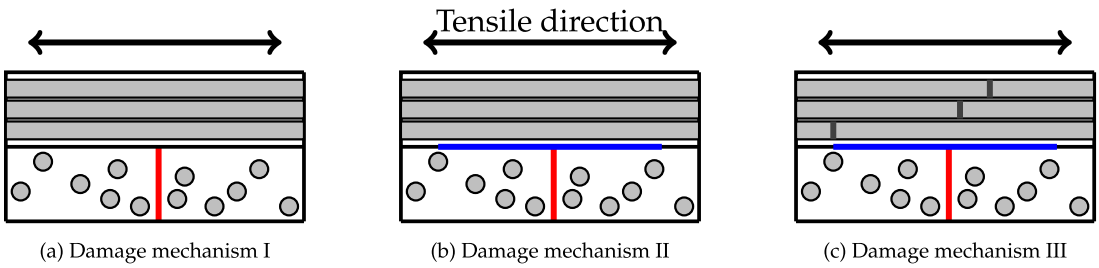

Fig. 1. The three damage mechanisms in fiber-reinforced composites under tension. I: Tunneling cracks (red) are initiated and propagate in off-axis layers. II: The stress concentrations due to the tunneling cracks initiate delamination cracks (blue) between off-axis layers and load-carrying layers. III: Fiber fracture (dark gray) of the load-carrying fibers leads to a major loss in strength and final failure. (For interpretation of the references to color in this figure legend, the reader is referred to the web version of this article.)

variational approaches are compared. Furthermore, a multitude of approaches exists, that analyze the problem under plane strain conditions (e.g. [9–12]), with the major limitation of only being applicable to cracks oriented at 90° relative to the main tensile direction. Hence, off-axis orientations cannot be considered.

The major novel contribution by the present work is the inclusion of arbitrary fiber and tunneling crack angles for predicting stiffness degradation due to tunneling cracks and delamination. This is done by a new 2D off-axis finite element framework which is applicable to general laminate lay-ups and fiber orientations, while still making use of efficient 2D computational models. The model includes the effect of frictionless contact between the tunnel-crack surfaces. An effect which is neglected in earlier studies [4–8] but turns out to have significant implications for the carbon fiber composite case for off-axis angles below 40°.

2. Problem

The stiffness degradation resulting from tunneling cracks and delamination (the damage mechanisms I and II in Fig. 1), in a uni-axially loaded symmetric and initially balanced laminate with layup $[0/\theta/0/-\theta]_s$ is considered. This is the same layup that was investigated in [13–15]. The tunneling cracks are all oriented in the same direction, which is given by the fiber orientation θ. With the convention that layers with tunneling cracks are denoted by a subindex c, a centrally cracked laminate as studied in the present paper may be denoted by $[0/\theta/0/-\theta_c]_s$.

The laminate is illustrated in Fig. 2 in a top view with the in-plane coordinates x_1 and x_3. A second in-plane coordinate system aligned with the tunneling cracks, i.e. aligned with the fibers, denoted by x_L and x_T, is also shown. In the case of tunneling and delamination cracks, a steady-state condition can be assumed, when the tunneling cracks are only oriented in a single direction and the edge effects of the laminate are neglected. This is a reasonable assumption as long as the length and width of the laminate are much greater than the height. Thus, well away from the edges, the stress and strain fields are invariant with respect to the x_L-axis, which is oriented along the tunnel cracks marked in red. Hence, the problem is essentially a 2D problem even for arbitrary angles θ.

As symmetric laminates are considered in this work only one-half of the laminate height is analyzed as illustrated in Fig. 3 by the top blue horizontal dashed symmetry line. The framework can however be applied to arbitrary layups, including asymmetric layups. In the presented work, all the layer heights are identical and denoted by h. The half-height of the laminate is denoted by H and the half-height of the crack is h_c. A uniform tunneling crack distribution is assumed, and the crack spacing is denoted by L, in good agreement with experimental observations in [16,17]. A corresponding crack density, $\rho_c = 1/L$, may be defined and will henceforth be used to specify the crack spacing. This assumption of equidistant cracks is made to simplify the model.

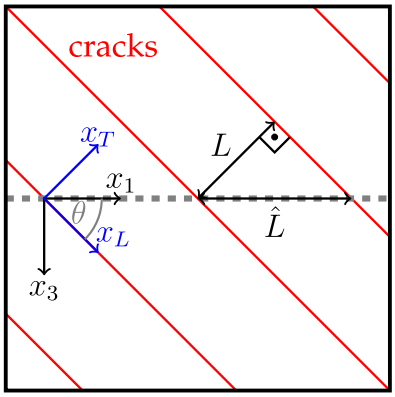

Fig. 2. Top view in the (x_1, x_3)-plane showing the periodic cracks in red, the distances between the cracks L, $\hat{L}$ and the global and local coordinate systems.

Nevertheless, this is not inherent to the modeling framework, which can handle any arbitrary crack distribution. In the tensile direction x_1 the distance between tunnel cracks is $\hat{L} = L/\sin(\theta)$ (see Fig. 2). By exploiting the symmetries of the problem an efficient computational model of length $\hat{L}/2$ is analyzed as shown in Fig. 3 marked by blue vertical dashed lines.

The delamination caused by the stress concentrations of the tunneling cracks is introduced at the tips of the tunneling cracks and it is assumed to extend along with the neighboring interfaces indicated in blue in Fig. 3. The two symmetry planes shown in Fig. 3 indicate that the delamination assumed is also symmetric and occurs in the dominant so-called H-shape, as discussed in [16]. For simplicity, this work only considers H-shaped delamination to showcase the abilities of the presented framework. The ability of the presented model to predict the degradation is however independent of the crack shapes. Any crack shape, possibly obtained by a simulation or experiment can be used as input to the model resulting in the corresponding stiffness degradation.

3. Numerical method

To capture the 3D effects of arbitrarily oriented off-axis cracks in a 2D model, the formulation from [15] is exploited. This 2D technique has been thoroughly validated against full 3D simulations in [15]. The isoparametric quadratic quadrilateral serendipity element used is shown in Fig. 4 with the natural coordinates (ξ, η). In this formulation, the geometry is defined on a 2D-plane, while the conventional displacement degrees of freedom (u_1, u_2, u_3) act in three dimensions. The off-axis deformations, due to e.g. off-axis cracks, can be captured with

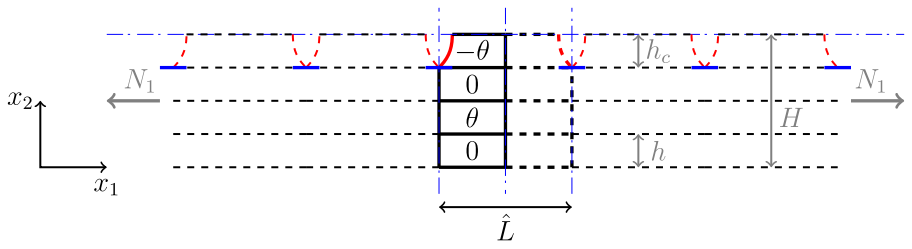

Fig. 3. Lower half of the deformed laminate $[0/\theta/0/-\theta_c]_s$ under a uni-axial tension load N_1 illustrating the periodicity and symmetry lines. The top horizontal blue dashed line indicates symmetry, whereas the vertical blue dashed lines indicate anti-symmetries. (For interpretation of the references to color in this figure legend, the reader is referred to the web version of this article.)

the following kinematic formulation, derived in [15],

$$\begin{aligned}
\varepsilon_{11} &= u_{1,1} \\
\varepsilon_{22} &= u_{2,2} \\
\gamma_{12} &= u_{1,2} + u_{2,1} \\
\gamma_{13} &= \bar{\gamma}_{13} + \cot(\theta)\cdot\bar{\varepsilon}_{11} - \cot(\theta)\cdot u_{1,1} + \tilde{u}_{3,1} \\
\gamma_{23} &= \bar{\gamma}_{23} + \tfrac{1}{2}\cot(\theta)\cdot\bar{\gamma}_{12} - \cot(\theta)\cdot u_{2,1} + \tilde{u}_{3,2} \\
\varepsilon_{33} &= \bar{\varepsilon}_{33} - \cot(\theta)\cdot\tilde{u}_{3,1}
\end{aligned} \tag{1}$$

where $\bar{\varepsilon}_{11}, \bar{\gamma}_{12}, \bar{\gamma}_{13}, \bar{\gamma}_{23}, \bar{\varepsilon}_{33}$ are the far-field strains, originating from the imposed far-field loading. In the finite element formulation, these are treated as five additional degrees of freedom to each element, as shown in red in Fig. 4. During the assembly these degrees of freedom are combined, yielding a single far-field strain field for the entire model. Hereby, it is possible to establish a full 3D strain tensor $\boldsymbol{\varepsilon}$ from a given displacement field $\boldsymbol{u}$ and the far field strains $\bar{\boldsymbol{\varepsilon}}$. In the context of finite elements, the special kinematics are imposed via the strain–displacement matrix, as presented in Eq. (2) of the summary box 1.

Summary 1: The special off-axis finite element [15]

The strain–displacement matrix for M nodes per element

$$\boldsymbol{B} = \begin{bmatrix}
N_{1,1} & 0 & 0 & \dots & N_{M,1} & 0 & 0 & 0 & 0 & 0 & 0 \\
0 & N_{1,2} & 0 & \dots & 0 & N_{M,2} & 0 & 0 & 0 & 0 & 0 \\
N_{1,2} & N_{1,1} & 0 & \dots & N_{M,2} & N_{M,1} & 0 & 0 & 0 & 0 & 0 \\
-c' N_{1,1} & 0 & N_{1,1} & \dots & -c' N_{M,1} & 0 & N_{M,1} & c' & 0 & 1 & 0 & 0 \\
0 & -c' N_{1,1} & N_{1,2} & \dots & 0 & -c' N_{M,1} & N_{M,2} & 0 & \tfrac{1}{2}c' & 0 & 1 & 0 \\
0 & 0 & -c' N_{1,1} & \dots & 0 & 0 & -c' N_{M,1} & 0 & 0 & 0 & 0 & 1
\end{bmatrix} \tag{2}$$

The 3D strain computation with the strain–displacement matrix

$$\begin{aligned}
&\boldsymbol{\varepsilon} = \boldsymbol{B}\boldsymbol{D} \\
&\boldsymbol{\varepsilon}^{\mathrm{T}} = \{\varepsilon_{11}, \varepsilon_{22}, \gamma_{12}, \gamma_{13}, \gamma_{23}, \varepsilon_{33}\}^{\mathrm{T}} \\
&\boldsymbol{D}^{\mathrm{T}} = \{u_1^{(1)}, u_2^{(1)}, \tilde{u}_3^{(1)}, \dots u_1^{(M)}, u_2^{(M)}, \tilde{u}_3^{(M)}, \bar{\varepsilon}_{11}, \bar{\gamma}_{12}, \bar{\gamma}_{13}, \bar{\gamma}_{23}, \bar{\varepsilon}_{33}\}^{\mathrm{T}}
\end{aligned} \tag{3}$$

The far-field strains are global quantities and only increase the entire domain by one degree of freedom per strain component. They can be computed in two ways. Either via an elimination using a direct prescription, as in [15], where the strains were computed prior to the finite element computation using classical laminate theory, or by using the far-field strain work-conjugate, i.e. the total far-field force $\bar{\boldsymbol{N}}$. Given a far-field force $\bar{\boldsymbol{N}}$, e.g. in a uni-axial out-of-plane loading scenario, the force N_3 applied in the x_3 direction, the far-field strains can be computed. There is a slight distinction between the in-plane and out-of-plane far-field forces, as the out-of-plane field was defined as a fluctuation field in [15]. In the out-of-plane direction x_3, the total far-field force is simply the total applied force in the out-of-plane direction x_3, whereas in the in-plane directions x_1 (and x_2), the total far-field force should be zero, as the loads are applied through conventional inhomogeneous finite element boundary conditions. As this work considers heavily damaged composites, the strain-field cannot

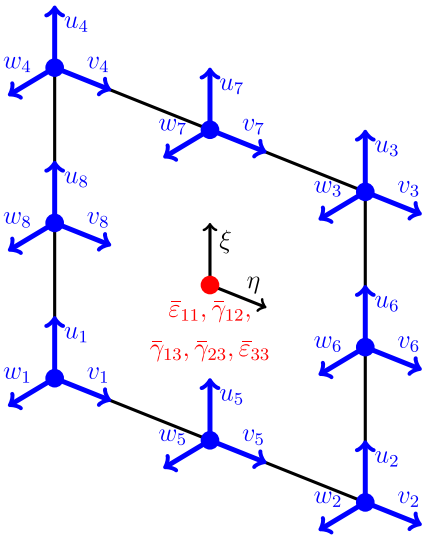

Fig. 4. The off-axis element as a quadratic quadrilateral serendipity element. (For interpretation of the references to color in this figure legend, the reader is referred to the web version of this article.)

be precomputed in an analytical manner. Hence, the second approach has to be used.

Due to the special off-axis formulation, the stiffness degradation due to arbitrarily oriented tunnel cracks can be modeled on a 2D plane, indicated by the gray dashed line in Fig. 2 and shown in detail in the (x_1, x_2)-plane in Figs. 3 and 5. Note, that the framework is only able to handle cracks oriented in the same (off-axis) direction. In the case of multiple crack orientations, the framework is still useful if the cracks are separated by a sufficiently large uncracked layer, e.g. a stiff load-carrying layer, as the crack interaction diminishes, as shown in [8] with parametric studies. Then the influence of the individual cracks on the stiffness can be analyzed separately and superimposed.

The periodicity of the problem is enforced by appropriate anti-symmetry boundary conditions at the vertical edges of the computational model, which restrict the out-of-plane displacement indicated by the red crosses, while maintaining straight vertical sides. On the left edge, the straightness is ensured by the homogeneous Dirichlet boundary conditions, whereas the right edge uses multi-point constraints to ensure, that the displacement in the x_1-direction are equal to the displacement of a reference node u_{ref} which is added to the finite element model. The axial force N_1 is then applied at the reference node. The validity of the boundary conditions has been verified by a comparison with a very large model including 100 cracks.

In the finite element model, the delamination, which is shown in blue in Fig. 5(a) is implemented via a 'seam', which disconnects the meshes between the interfaces. The extent of the delamination is given by the dimensionless delamination ratio, $d_r \in [0; 1[$, such that d_r is zero for no delamination and unity for a full separation of the plies.

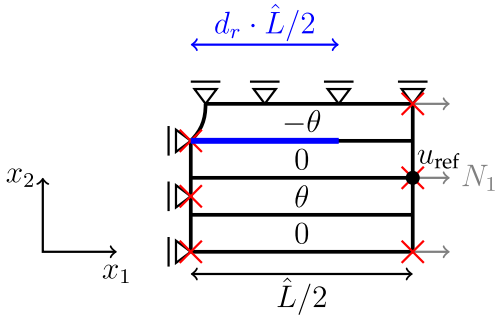

(a) The model with its symmetry boundary conditions. The roller supports restrict the degrees of freedom in the x_1 or the x_2 directions, whereas the red crosses mark the restriction of displacements in the x_3 direction (out of plane). The gray arrows indicate the prescribed axial load N_1. The delamination is marked in blue.

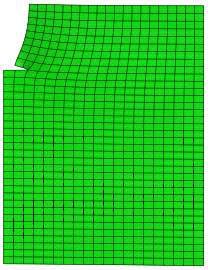

(b) Illustration of a typical 2D mesh with 720 quadratic quadrilateral elements in its deformed state. This is found for an orientation $\theta = 60°$, a crack density of $\rho_c H = 1$ and a delamination ratio $d_r = 0.1$ with the material GlassFRP.

Fig. 5. The deformed periodic model and its discretization exploiting the symmetries illustrated in Fig. 3. (For interpretation of the references to color in this figure legend, the reader is referred to the web version of this article.)

Fig. 5(b) shows a typical deformed finite element mesh. This specific mesh uses 720 quadratic quadrilateral elements leading to convergence errors on the total laminate stiffness smaller than 0.05% when compared to a converged solution using up to half a million elements. Despite the stress concentration due to the tunnel crack tip and delamination crack tip, the reaction forces at the outer edges have a low sensitivity with respect to the mesh size, leading to a relatively low requirement on the discretization. If crack propagation computations were however considered a better discretization at the crack tips would be required, as employed in [15]. A typical runtime for these relatively coarse cases with 500–1000 elements lies in the range of a few seconds for the model on a single core of an AMD EPYC 7351 (2.9 GHz) processor. The computational demand decreases for greater crack densities, i.e. smaller crack spacings, L, as fewer elements are needed.

A user subroutine implementation together with Python scripts is available at [18], that is to be run through Abaqus, and can represent any arbitrary symmetric laminate layup.

4. Validation

The periodic model shown in Fig. 5a is validated against several cases from the literature. An overview of the validation cases is provided in Table 1, which contains semi-analytical, numerical, as well as experimental cases. All layups are symmetric and have cracks oriented in only a single direction, as the off-axis framework cannot handle multiple orientations without further computations. The crack density ρ_c, commonly expressed in number of cracks per millimeter, will always be defined in non-dimensional form with the total laminate height as $\rho_c H$.

The axial stiffness in the x_1-direction, E_1, is extracted based on the geometrical properties, H, L, and θ, the prescribed displacement in the x_1-direction, u_1, and the applied load per unit width of the laminate plate, N_1 [N/m], as

$$E_1 = \frac{N_1/H}{u_1/(\hat{L}/2)} = \frac{N_1 L}{2 H u_1 \sin(\theta)}. \tag{4}$$

The damaged stiffness value will be normalized by the undamaged value, E_1^0. This can either be calculated based on classical laminate theory or the presented finite element model without defects. In this work, the classical laminate theory estimate is used.

An important application of the classical laminate theory is the estimation of a lower stiffness degradation bound, known as the ply-discount method (see e.g. [19]), which can be based on different modeling choices. Either the damaged ply can be assumed to lose its entire stiffness or it can be assumed to only lose its local transverse and shear stiffness while retaining its longitudinal stiffness along the tunneling crack direction (see e.g. [20]), which is implemented by setting E_T and G_{LT} to zero in the damaged ply. The latter is found to provide better agreement with numerical results [19], and it will therefore be used as a limiting case in the present study. Henceforth, it will be referred to as *the ply discount estimate*. The former traditional approach of neglecting the entire stiffness of the ply can be considered as an ultimate bound, that is not to be breached by any simulation results. Nevertheless, it often leads to a very conservative bound which is not the case for the ply discount estimate used here.

First, the cases with tunneling cracks oriented at $\theta = 90°$ [4,6] are considered. In Ref. [6] a comparison is made to values from experiments, whereas [4] includes a comparison to an analytical approach, called the stress transfer model. Note that two different layups and material systems are used in these studies. A comparison in terms of the normalized axial stiffness is provided in Figs. 6(a) and 6(b), for experimental and numerical results, respectively. A good agreement is observed for the experimental results (Fig. 6(a)), and slight deviations occur for greater crack densities, especially compared to the analytical stress transfer model [4] (Fig. 6(b)). The errors in the total laminate stiffness are, however, below 0.04%. Convergence towards the ply discount estimate shown by the horizontal dashed line occurs for both cases.

While the former cases may be treated in a generalized 2D plane strain framework, the case of $\theta = 45°$ tunnel cracks investigated by [21,23] can traditionally only be treated by 3D simulations. Here, however, the case with cracks in the $\theta = 45°$-direction can be solved by the specialized 2D model using the present off-axis finite element framework. A comparison with experimental values as well as 3D periodic finite element results from [22] is shown in Fig. 7(a), and a good agreement is observed. Thus, it is seen that the 2D framework can model unbalanced layups representing in-plane coupling effects. Also for this case a convergence towards the ply discount estimate is evident. Fig. 7(b) shows results from [22] compared to results obtained based on the present off-axis finite element framework, and a good agreement is also seen here for the layup $[0/45_c/-45]_s$.

Finally, the 3D finite element model by [20] is used as a validation case, where a greater range of tunneling crack densities is explored reaching up to $\rho_c H = 10^3$. Two tunnel crack orientations of $\theta = 55°$ and $\theta = 70°$ are investigated, as illustrated in Fig. 8. A very strong agreement between the highly efficient 2D off-axis finite element models and the computationally heavy 3D models are observed. Also here, it is seen that at high crack densities, the ply discount estimate is reached.

Table 1
Five different validation cases with type, layup, material properties and ply thickness. Note that the subindex c in the layup definition indicates the ply containing the tunneling crack. The delamination cracks always occur between the layers with tunneling cracks and the layers without.

Validation case	[6]	[4]	[21]	[22]	[20]
Type	Experimental	Analytical	Experimental	Numerical	Numerical
Layup	$[\pm\theta/90_{4_c}]_s$	$[\pm 45/0/90_c]_s$	$[0/45_c]_s$	$[0/45_c]_s$ $[0/45_c/-45]_s$	$[0/\theta_{4_c}/-\theta_4/0_{1/2}]_s$
E_L [GPa]	44.73	136.6	43.00	48.83	44.70
$E_T = E_{T'}$ [GPa]	12.76	9.790	13.00	14.07	12.70
$G_{LT} = G_{LT'}$ [GPa]	5.800	6.474	4.690	5.200	5.800
$G_{TT'}$ [GPa]	4.490	3.364	4.643	5.025	4.500
$\nu_{LT} = \nu_{LT'}$ [-]	0.297	0.286	0.300	0.308	0.297
$\nu_{TT'}$ [-]	0.420	0.455	0.400	0.400	0.411
Ply thickness [mm]	0.144	0.125	0.610 in 45°-ply[a] 0.640 in 0°-ply	0.600	0.144

[a]The ply thickness information is found in [23].

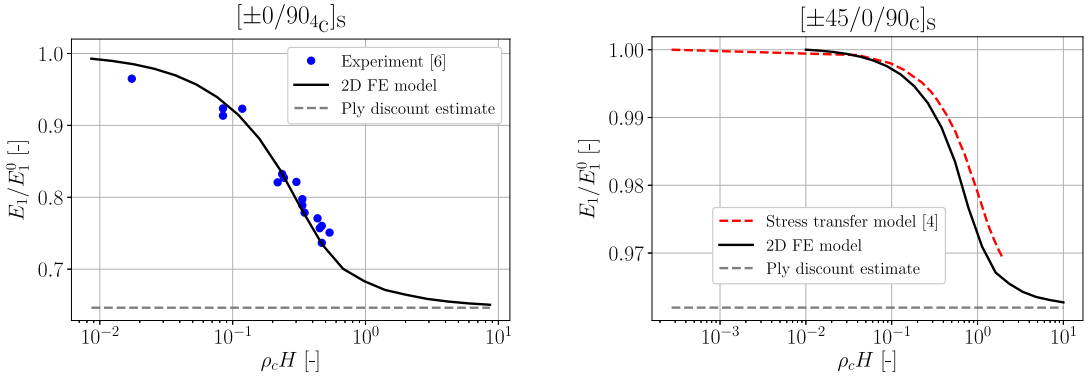

(a) Comparison to experiment from [6].

(b) Comparison to analytical stress transfer model from [4].

Fig. 6. Stiffness degradation validation case with cracks orientated at 90°.

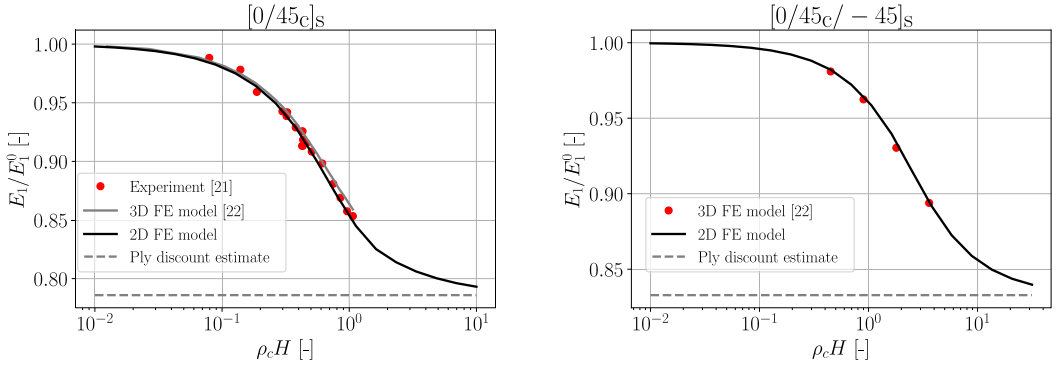

(a) Comparison with experimental values from [21] and to results from a periodic 3D Finite element model by [22]

(b) Comparison with values obtained with a periodic 3D Finite element model by [22].

Fig. 7. Stiffness degradation validation case with crack orientated at 45°.

The focus is now shifted to cases where delamination also occurs. Results for a $[0/45_c/-45]_s$ layup are compared to the 3D periodic finite element results presented in [22]. Delamination cracks at the interfaces near the tunneling cracks, between the 0° and 45° layers ($[0/45_c]$), and between the 45° and −45° layers ($[45_c/-45]$) are modeled. The results are presented in Fig. 9 as a function of normalized delamination area d_r, where the red symbols are results from the 3D finite element model by [22] and the black lines are results from the present 2D off-axis finite element model. The agreement is here better than 0.2% comparing the total laminate stiffness's.

5. Results

The model is now applied to the more general layup $[0/\theta/0/-\theta_c]_s$ for the materials GlassFRP and CarbonFRP presented in Table 2, which are also considered in [14,15]. Such cases with a general fiber and crack orientation given by θ_c have not been investigated previously in the

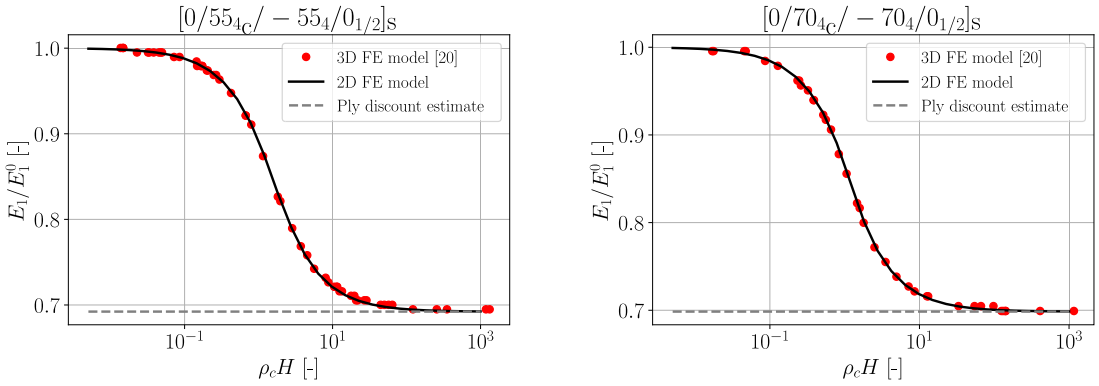

(a) $\theta = 55°$. (b) $\theta = 70°$.

Fig. 8. Comparison of the present model to values obtained with a periodic finite element model by [20] using the layup $[0/\theta_{4_c}/-\theta_4/0_{\frac{1}{2}}]_s$.

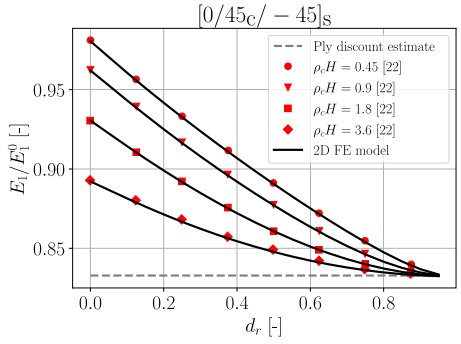

Fig. 9. Comparison of stiffness degradation, with values obtained with a periodic 3D finite element by [22] using the layup $[0/45_c/-45]_s$. The stiffness degradation is shown as a function of the delamination ratio.

Table 2
Material properties used for glass or carbon fiber reinforced polymers.

Material	E_L	$E_T = E_{T'}$	$G_{LT} = G_{LT'}$	$G_{TT'}$	$\nu_{LT} = \nu_{LT'}$	$\nu_{TT'}$
Unit	GPa	GPa	GPa	GPa	–	–
GlassFRP	30.62	8.62	3.25	2.90	0.29	0.33
CarbonFRP	266.0	5.49	3.54	2.37	0.27	0.40

literature. To showcase the capabilities of the novel model, multiple parametric studies are conducted and presented.

5.1. Damage stage I: Tunnel-cracking

Fig. 10 shows the stiffness degradation, caused by an increasing tunneling crack density where results for both GlassFRP (Fig. 10a) and CarbonFRP (Fig. 10b) are presented for three orientations $\theta = 30°$, $\theta = 60°$, and $\theta = 90°$. For both materials, the convergence toward the ply discount estimate is clear.

One important aspect neglected by previous models and the computation presented in Fig. 10 is the potential contact occurring at the tunnel cracking surfaces. The bounds of this effect on the stiffness degradation can easily be extracted from the proposed model. Obviously, no stiffness degradation occurs in the situation of full contact with sticking friction along the crack surfaces. However, for a lower bound stiffness estimation, a frictionless contact can be considered. This can be included in the model by imposing boundary conditions at the crack, constraining normal separation (along x_T in Fig. 2) while imposing vanishing shear tractions along the crack surfaces (along x_L in Fig. 2). Such frictionless contact is achieved by a multi-freedom constraint for each node along the free crack surface. With this extension it is not only possible to determine a lower bound of the degraded stiffness, but it is also possible to determine the situations in which contact occurs. This would be the case for positive reaction forces at the constrained crack face nodes indicating compression and thereby crack face contact. On the other hand, in the case of negative reaction forces along the entire crack surface, the crack would open and the special contact constraint should not be considered. The intermediate situation, where the reaction forces for the constrained crack surfaces have varying signs, a partial contact is likely. A similar estimate can be made with the contactless model used for the former validation cases, where the overlap of the fracture surfaces is considered in terms of u_n along the crack height. If an overlap at all nodes occurs, it is considered a full contact situation. Similarly, a partial contact may by found. Note, that the two different assessment methods do not produce identical results and only provide an estimate to the transition zone from full contact to no contact.

An initial assessment for the layup $[0/\theta/0/-\theta_c]_s$ is presented in Fig. 11 for both GlassFRP and CarbonFRP. Here, the range of orientations θ, where contact occurs are investigated and the difference between the results for the frictionless contact formulation (marked with solid thick lines) and the contactless formulation (marked with solid thin lines) is illustrated. The circular marks indicate a full contact, whereas the crosses indicate partial contact. In the case of GlassFRP, no large deviations occur for the full contact situation, while differences are observable for partial contact. However, this only occurs for the larger values of θ, where the contact is minimal, which means that the entire stiffness degradation curve is captured well by the contactless formulation. On the other hand, for CarbonFRP, the two models give significantly different results, showing that contact must be considered. Furthermore, the transition zone can be identified, where the partial contact occurs. Here, one model seems to take over from the other. For small angles, θ, there is full contact (circles). For increasing angles there is first partial contact (crosses) and then at even larger angles there is full crack opening. Thus, the thin solid line without crosses indicates a contactless solution without any crack-surface penetration. The transition zone is not rigorously modeled, but the deviations between the two different estimates are small for partial contact.

Henceforth, a combination of the models is used, such that the frictionless contact model is employed for full contact and the contactless model is employed for no contact, while the intermediate regime is modeled using both approaches.

Returning to the stiffness degradation presented in Fig. 10, it is observed, that for GlassFRP the stiffness degradation is modest for $\theta = 30°$, which might be expected, due to the local longitudinal stiffness not being affected as much for smaller angles. Interestingly, the opposite occurs for CarbonFRP, where the greatest stiffness degradation occurs for $\theta = 30°$. To study this phenomenon, a parametric study of the

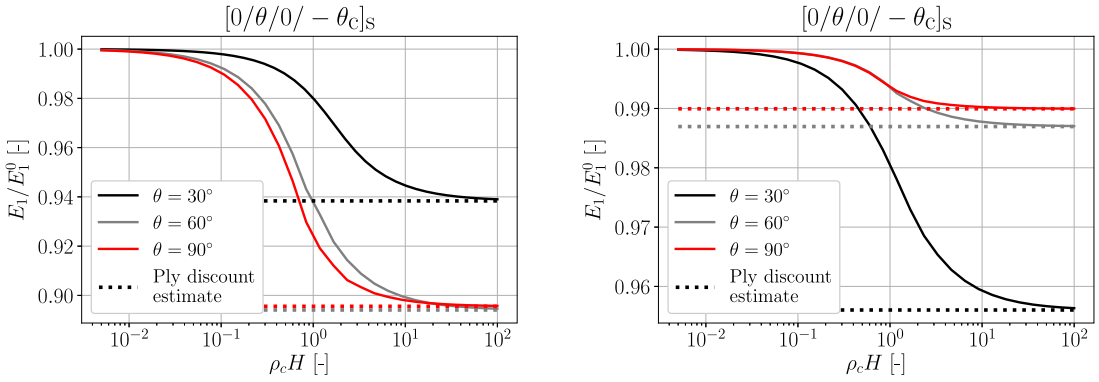

(a) GlassFRP. (b) CarbonFRP.

Fig. 10. Influence of the tunneling crack density ρ_c on the stiffness degradation for the layup $[0/\theta/0/-\theta_c]_s$.

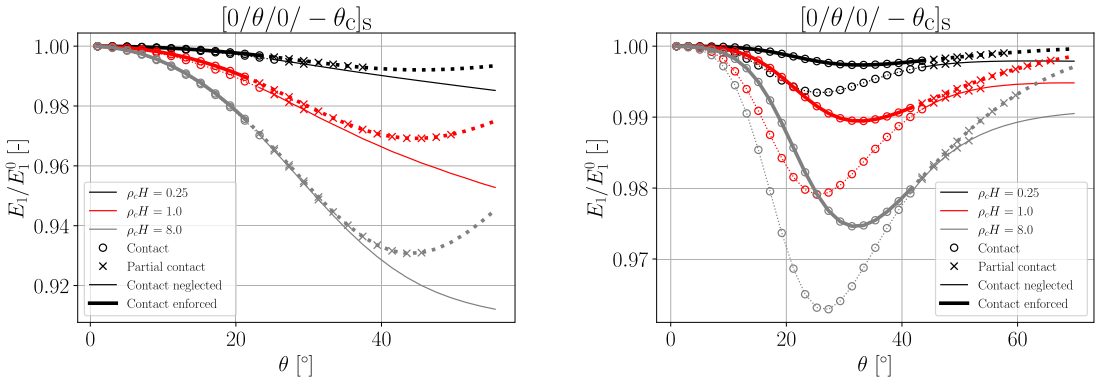

(a) GlassFRP (b) CarbonFRP

Fig. 11. Comparison of the frictionless contact formulation, marked with solid thick lines and the contactless formulation, marked with solid thin lines. The circle marks indicate a full contact of the crack surfaces, whereas the crosses indicate a partial contact. The results are presented for various orientations θ tunneling crack densities $\rho_c H$.

stiffness degradation with respect to the orientation θ is performed, where the results are presented in Fig. 11. A lower stiffness degradation at very small angles is confirmed. For CarbonFRP, the maximal stiffness degradation occurs at about $\theta \approx 30°$. This is in contrast to GlassFRP where a continuous stiffness degradation is seen for increasing values of θ as observed in Fig. 11a.

As indicated in Fig. 11 (circles mark full contact and crosses mark partial contact), contact between the tunneling crack faces was observed at small angles. This observation is in agreement with the results obtained in [14,15].

5.2. Damage stage II: Delaminations

In addition to the tunneling cracking, delamination cracks may develop as sketched in Fig. 1(b). This will result in further stiffness degradation. The influence of the orientation θ on the ensuing stiffness degradation is investigated given different delamination ratios, d_r, and crack densities, ρ_c. For the CarbonFRP case results are shown for a lower tunnel crack density of $\rho_c H = 0.5$ and a higher tunnel crack density of $\rho_c H = 4$ in Fig. 13a and b, respectively. A similar stiffness degradation as a function of angle as in Fig. 12b is observed. For a greater tunneling crack density, ρ_c, the differences between the different delamination ratios are smaller, as a significant amount of the stiffness is already lost due to the tunneling cracks. Thus delamination can only have a large impact on the stiffness at lower tunnel crack densities. Note, that only the contact of the tunneling crack surfaces is considered. Contact may also arise at the delamination surfaces, but this is not considered in this work, as it was previously shown by [16] to have a negligible influence.

In the following, an approach is proposed for how the model can be applied to defect detection in laminates. For simplicity, GlassFRP is used, where the contact influence is negligible as shown in Fig. 11(a). For this approach two stiffness degradation curves of the layup $[0/\theta/0/-\theta_c]_s$ are provided in Fig. 14, where Fig. 14(a) shows the axial and Fig. 14(b) the transverse stiffness degradation. The transverse stiffness is computed by rotating the laminate by 90°, i.e. using the layup $[90/\theta + 90/90/ - \theta + 90_c]_s$, and applying an in-plane axial load. Given two stiffness measurements, one in the axial and one in the transverse direction, a comparison with the graphs in Fig. 14 may be used to identify the tunneling crack density. This is done under the assumption that no other damage mechanisms are present. Nevertheless, if a discrepancy is observed, this is an indication for the presence of other damage mechanisms, e.g. delamination cracks.

The combined influence of the tunneling cracks and the delamination cracks can be quantified systematically in the form of the contour plot, shown in Fig. 15. The black lines indicate the contours of the axial stiffness degradation, whereas the red lines indicate the transverse stiffness degradation. Based on this figure, if the axial stiffness degradation and the tunneling crack density are known, the delamination ratio can be identified. Alternatively, given two simultaneously orthogonal stiffness measurements both the tunneling crack density and the delamination ratio can be identified.

As an example to illustrate this, consider a stiffness degradation measurement in the x_1-direction of 0.972, and in the x_3-direction of 0.875 for the GlassFRP composite. Using Fig. 15, a tunneling crack

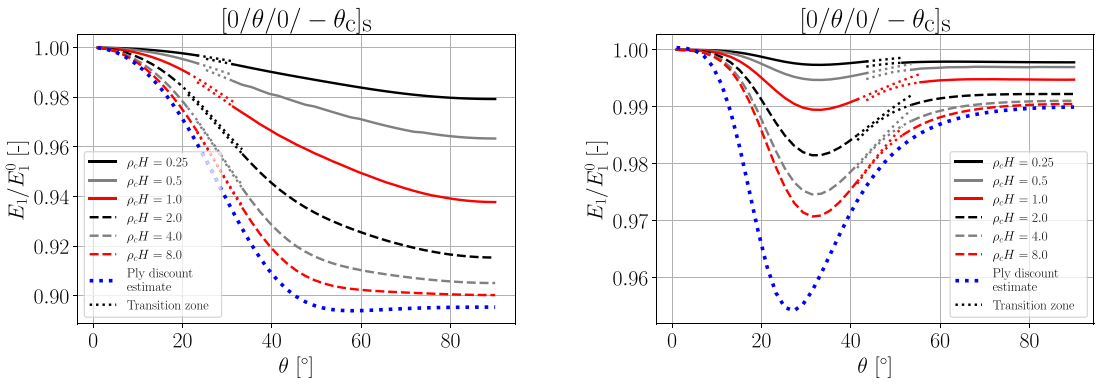

(a) GlassFRP. (b) CarbonFRP.

Fig. 12. Influence of the orientation θ on the axial stiffness degradation for different tunneling crack densities, ρ_c.

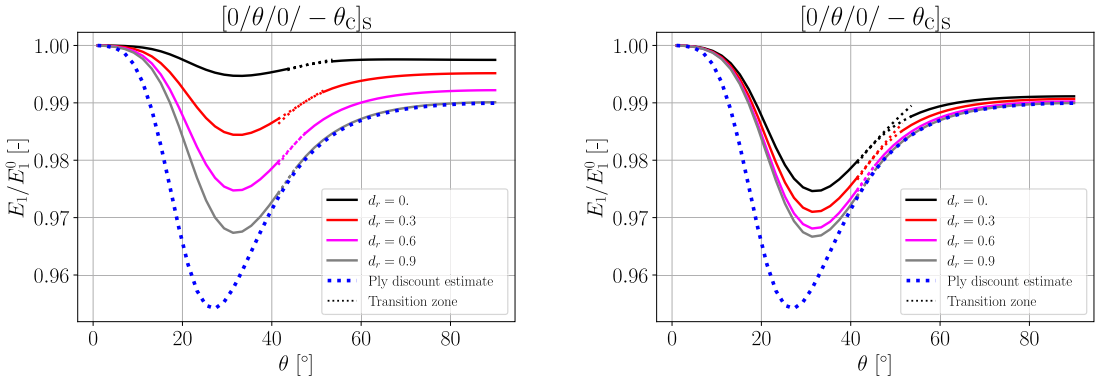

(a) $\rho_c H = 0.5$ (b) $\rho_c H = 4$

Fig. 13. Influence of the orientation θ, the tunneling crack density ρ_c and the delamination ratio d_r on the stiffness degradation for the layup $[0/\theta/0/-\theta_c]_s$ with the material CarbonFRP.

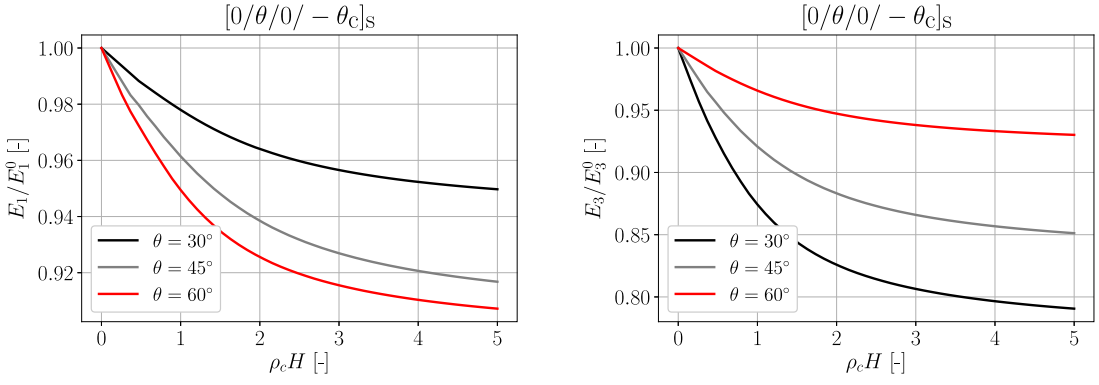

(a) Axial stiffness degradation E_1. (b) Transverse stiffness degradation E_3.

Fig. 14. Stiffness degradation for different tunneling crack densities, ρ_c, for the layup $[0/\theta/0/-\theta_c]_s$. Both axial E_1 and transverse E_3 stiffnesses are considered. The material is GlassFRP.

density of $\rho_c H = 0.16$ and a delamination ratio of $d_r = 0.375$ can uniquely be identified. Hence, there are 0.16 tunneling cracks per laminate height H and a delamination of 37.5% of the interface. Note, that interpolations between the contours will be needed in general.

As a note on computational efficiency, the $24 \times 24 = 576$ data points in Fig. 15, which corresponds to 576 individual finite element simulations, were created in about 3 h on a single core of an AMD EPYC 7351 (2.9 GHz) processor. The corresponding full 3D analyses would require several orders of magnitude more in computational resources.

5.3. Damage stage III: Fiber fracture

For simplicity, the stiffness degradation due to the final fiber fracture has not been included in the model. Nevertheless, the fiber breakage zone is typically aligned with the tunnel-crack orientation [2,24,

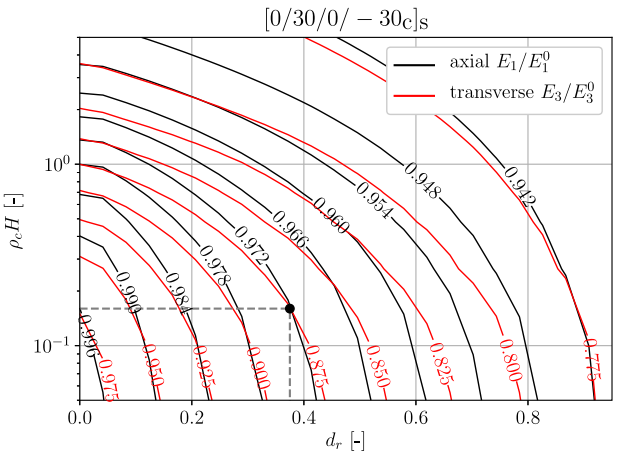

Fig. 15. The stiffness degradation of the layup $[0/30/0/-30_c]_s$ in the axial direction marked in black and in the transverse direction marked in red is shown. The material is GlassFRP. (For interpretation of the references to color in this figure legend, the reader is referred to the web version of this article.)

25], and the stiffness degradation could efficiently be included inside the 2D off-axis finite element framework by relating the density of uni-axial fiber breakage with the stiffness degradation.

6. Conclusion

A recently developed 2D off-axis finite element framework [15] has been applied to accurately predict the axial and transverse stiffness degradation caused by tunneling cracks existing simultaneously with delamination cracks. The model is extended with a basic contact formulation without increasing the computational cost. This enables both identifying contact situations and assessing their maximum and minimum influence on the stiffness degradation. A periodic model with a fairly general layup is considered throughout the paper, e.g. $[0/\theta/0/-\theta_c]_s$, where the subscript 'c' indicates the layer with tunneling cracks. A good agreement with a variety of analytical, 3D numerical, and experimental cases from literature has been demonstrated as validation of the model. The Fortran-based user-subroutine and Python implementation of the model in the commercial code Abaqus, which can represent any arbitrary layup, have been made available in a fairly "plug and play" version at [18].

Through numerical simulations, it has been demonstrated that the novel 2D off-axis finite element model is highly efficient and provides results in agreement with experimental observations as well as previous 3D studies from the literature. Typical simulations take seconds, and very large parametric studies are carried out in a few hours.

Multiple new parametric studies were performed to showcase the capabilities of the proposed model, which are useful during the design process to avoid problematic stiffness degradations. Such knowledge is also useful during monitoring of structures, where the progression of the internal damage can be assessed via the stiffness degradation. For a particular material system the stiffness degradation and the associated damage in terms of tunneling cracks and delamination can be evaluated and assessed from results as those presented in Fig. 15 for GlassFRP laminate with the layup $[0/30/0/-30_c]_s$.

Despite the limitations of the 2D off-axis framework to modeling cracks oriented only in a single direction, the effect of multiple crack orientations on a laminates' stiffness degradation can be taken into account if neglecting the cross-ply interaction between the cracks. This is realistic in cases where a stiff load-carrying layer is located in between, and the stiffness degradations from each of the orientations may then be superposed, as discussed in [8].

This work limits itself to the axial and transverse stiffness degradation but can, by modifying the loading scenarios estimate any linear elastic constitutive parameter. Any loading scenario, including bending and shear, can be handled by the 2D off-axis finite element framework including lower and upper estimates of the degradation with the current contact formulation. A better estimate of the degradation in the presence of contact can be obtained by employing a proper contact formulation, such as those summarized in [26], which still remains compatible with the off-axis framework.

CRediT authorship contribution statement

Leon Herrmann: Conceptualization, Data curation, Investigation, Writing – original draft, Writing – review & editing. **Lars P. Mikkelsen:** Conceptualization, Project administration, Writing – review & editing, Supervision. **Brian N. Legarth:** Conceptualization, Methodology, Supervision, Writing – review & editing. **Fabian Duddeck:** Supervision, Writing – review & editing. **Christian F. Niordson:** Conceptualization, Methodology, Supervision, Writing – review & editing.

Declaration of competing interest

The authors declare that they have no known competing financial interests or personal relationships that could have appeared to influence the work reported in this paper.

Data availability

We have shared the data in a zenodo link given in reference [18] in the manuscript.

References

[1] F. Crossman, A. Wang, The dependence of transverse cracking and delamination on ply thickness in graphite/epoxy laminates, in: K. Reifsnider (Ed.), Damage in Composite Materials: Basic Mechanisms, Accumulation, Tolerance, and Characterization, ASTM International, 1982, pp. 118–122, http://dx.doi.org/10.1520/STP34324S.

[2] R. Jamison, K. Schulte, K. Reifsnider, W. Stinchcomb, Characterization and analysis of damage mechanisms in tension-tension fatigue of graphite/epoxy laminates, in: Effects of Defects in Composite Materials, ASTM STP 836, American Society for Testing and Materials, 1984, pp. 21–55.

[3] J. Zhang, K.P. Herrmann, Stiffness degradation induced by multilayer intralaminar cracking in composite laminates, Composites A 30 (5) (1999) 683–706, http://dx.doi.org/10.1016/S1359-835X(98)00106-7.

[4] L.N. McCartney, Stress transfer mechanics for ply cracks in general symmetric laminates, Technical Report, National Physical Laboratory (Great Britain), Centre for Materials Measurement & Technology, 1996.

[5] J. Varna, R. Joffe, N.V. Akshantala, R. Talreja, Damage in composite laminates with off-axis plies, Compos. Sci. Technol. 59 (14) (1999) 2139–2147, http://dx.doi.org/10.1016/S0266-3538(99)00070-6.

[6] R. Joffe, J. Varna, Analytical modeling of stiffness reduction in symmetric and balanced laminates due to cracks in 90° layers, Compos. Sci. Technol. 59 (11) (1999) 1641–1652, http://dx.doi.org/10.1016/S0266-3538(99)00025-1.

[7] P. Lundmark, J. Varna, Constitutive relationships for laminates with ply cracks in in-plane loading, Int. J. Damage Mech. 14 (3) (2005) 235–259, http://dx.doi.org/10.1177/1056789505050355.

[8] P.A. Carraro, M. Quaresimin, A stiffness degradation model for cracked multidirectional laminates with cracks in multiple layers, Int. J. Solids Struct. 58 (2015) 34–51, http://dx.doi.org/10.1016/j.ijsolstr.2014.12.016.

[9] P. Lundmark, J. Varna, Constitutive relationships for laminates with ply cracks in in-plane loading, Int. J. Damage Mech. 14 (3) (2005) 235–259, http://dx.doi.org/10.1177/1056789505050355.

[10] A.S.J. Suiker, N.A. Fleck, Crack tunneling and plane-strain delamination in layered solids, Int. J. Fract. 125 (1) (2004) 1–32, http://dx.doi.org/10.1023/B:FRAC.0000021064.52949.e2.

[11] J.L. Beuth, Cracking of thin bonded films in residual tension, Int. J. Solids Struct. 29 (13) (1992) 1657–1675, http://dx.doi.org/10.1016/0020-7683(92)90015-L.

[12] S. Ho, Z. Suo, Tunneling cracks in constrained layers, J. Appl. Mech. 60 (4) (1993) 890–894, http://dx.doi.org/10.1115/1.2900998.

[13] M. Quaresimin, P.A. Carraro, L.P. Mikkelsen, N. Lucato, L. Vivian, P. Brøndsted, B.F. Sørensen, J. Varna, R. Talreja, Damage evolution under cyclic multiaxial stress state: A comparative analysis between glass/epoxy laminates and tubes, Composites B 61 (2014) 282–290, http://dx.doi.org/10.1016/j.compositesb.2014.01.056.

[14] L.P. Mikkelsen, S.J. Klitgaard, C.F. Niordson, B.F. Sørensen, Tunneling cracks in arbitrary oriented off-axis lamina, Int. J. Fract. 226 (2) (2020) 161–179, http://dx.doi.org/10.1007/s10704-020-00485-9.

[15] L.P. Mikkelsen, B.N. Legarth, L. Herrmann, M.M. Christensen, C.F. Niordson, A special finite element method applied to off-axis tunnel cracking in laminates, Eng. Fract. Mech. 268 (2022) 108387, http://dx.doi.org/10.1016/j.engfracmech.2022.108387.

[16] P.A. Carraro, L. Maragoni, M. Quaresimin, Characterisation and analysis of transverse crack-induced delamination in cross-ply composite laminates under fatigue loadings, Int. J. Fatigue 129 (2019) 105217, http://dx.doi.org/10.1016/j.ijfatigue.2019.105217.

[17] K.M. Jespersen, Fatigue Damage Evolution in Fibre Composites for Wind Turbine Blades, DTU Wind Energy PhD-0075, Technical University of Denmark, 2017.

[18] L. Herrmann, L.P. Mikkelsen, B.N. Legarth, C.F. Niordson, An Efficient Stiffness Degradation Model for Layered Composites with Arbitrarily Oriented Tunneling and Delamination Cracks [Software], Zenodo, 2022, http://dx.doi.org/10.5281/zenodo.5730309.

[19] I.M. Daniel, O. Ishai, Engineering Mechanics of Composite Materials, Oxford University Press, 1994.

[20] E.J. Barbero, F.A. Cosso, F.A. Campo, Benchmark solution for degradation of elastic properties due to transverse matrix cracking in laminated composites, Compos. Struct. 98 (2013) 242–252, http://dx.doi.org/10.1016/j.compstruct.2012.11.009.

[21] D.T.G. Katerelos, L.N. McCartney, C. Galiotis, Effect of off – axis matrix cracking on stiffness of symmetric angle-ply composite laminates, Int. J. Fract. 139 (3) (2006) 529–536, http://dx.doi.org/10.1007/s10704-006-0100-9.

[22] L. Maragoni, P.A. Carraro, M. Quaresimin, Periodic boundary conditions for FE analyses of a representative volume element for composite laminates with one cracked ply and delaminations, Compos. Struct. 201 (2018) 932–941, http://dx.doi.org/10.1016/j.compstruct.2018.06.058.

[23] D.T.G. Katerelos, M. Kashtalyan, C. Soutis, C. Galiotis, Matrix cracking in polymeric composites laminates: Modelling and experiments, Compos. Sci. Technol. 68 (12) (2008) 2310–2317, http://dx.doi.org/10.1016/j.compscitech.2007.09.013.

[24] K.L. Reifsnider, R. Jamison, Fracture of fatigue-loaded composite laminates, Int. J. Fatigue 4 (4) (1982) 187–197, http://dx.doi.org/10.1016/0142-1123(82)90001-9.

[25] J. Zangenberg, P. Brøndsted, J.W. Gillespie, Fatigue damage propagation in unidirectional glass fibre reinforced composites made of a non-crimp fabric, J. Compos. Mater. 48 (2013) 2711–2727, http://dx.doi.org/10.1177/0021998313502062.

[26] P. Wriggers, Computational contact mechanics, Engineering Mechanics of Composite Materials, Springer Berlin, Heidelberg, 2006, http://dx.doi.org/10.1007/978-3-540-32609-0.